IAS SEDIMENTOLOGY
Journal of the International Association of Sedimentologists

Settling-driven convection limits the spatial scale of deposition beneath sediment-laden buoyant flows in lakes and the coastal ocean

Journal:	*Sedimentology*
Manuscript ID	Draft
Manuscript Type:	Original Manuscript
Date Submitted by the Author:	n/a
Complete List of Authors:	Davarpanah Jazi, Shahrzad; University of Toronto, Physical and Environmental Sciences Wells, Mathew; University of Toronto, Physical and Environmental Sciences
Keywords:	Settling-driven convection, Convective sedimentation, Particle-laden gravity current, Sediment-laden flow, Sediment fingering, Stokes settling velocity

Note: The following files were submitted by the author for peer review, but cannot be converted to PDF. You must view these files (e.g. movies) online.

MovieS1.wmv
MovieS2.wmv
MovieS3.wmv
MovieS4.wmv
MovieS5.wmv
MovieS6.wmv

Settling-driven convection limits the spatial scale of deposition beneath sediment-laden buoyant flows in lakes and the coastal ocean

Shahrzad Davarpanah Jazi and Mathew G. Wells
Department Physical & Environmental Sciences, University of Toronto
1065 Military Trail, M1C 1A4, Toronto, ON, Canada
Email: sh.davarpanahjazi@mail.utoronto.ca, Email: wells@utsc.utoronto.ca

ABSTRACT

The length-scale of deposition beneath a buoyant sediment-laden river plume can be strongly influenced by enhanced settling-driven convection, and is directly related to the horizontal velocity of the plume and a sedimentation time-scale. In our experiments, a buoyant plume of fresh water and sediment spreads over a denser saline layer. The speed of the plume increases with the net density difference between the layers, while in contrast, the time-scale of the settling-driven convection is related inversely to the density anomaly due to the sediment concentration difference. These competing effects result in the length-scale of propagation increasing as $L_{prop} \sim \sqrt{1 - 1/R_\rho}\, R_\rho^{2/3}$, where $R_\rho = \Delta\rho_S/\Delta\rho_C$ is the ratio of density differences due to salt and sediment. When R_ρ is close to one, settling-driven convection is vigorous and the propagation length-scale is very small. Beneath the surface plume, the descending sediment-laden fluid can also form an interflow or underflow, which is able to propagate greater distances than the surface plume. The implication of these results for sediment-laden river plumes in lakes and the coastal ocean are discussed.

Keywords: Settling-driven convection, Convective sedimentation, Particle-laden gravity current, Sediment-laden flow, Sediment fingering, Stokes settling velocity.

1. INTRODUCTION

When a sediment-laden river reaches a stratified lake or the coastal ocean, the subsequent distribution of sedimentary layers on the bed of the lake or coastal ocean is determined to a large extent by the rate which the river plume propagates laterally compared to the vertical settling rate of sediment. In the absence of strong winds or tides, the horizontal velocities of surface river plumes are largely determined by buoyancy forces (*Horner-Devine at al.,* 2015). While the dynamics of buoyant plumes are now quite well understood (*Yuan & Horner-Devine*, 2017), the studies of dynamics of sediment-laden gravity currents have primarily focused on dense currents that propagate along a bed (*Bonnecaze et al.,* 1993, *Meiburg & Kneller*, 2010). For these bottom currents, benthic turbulence can easily resuspend sediment into the main body of the current, so that they maintain their density anomaly for longer and travel large distances. In contrast, a buoyant surface plume will potentially lose all the particles beneath it within a finite distance. Previous experiments on buoyant surface sediment-laden plumes (*Maxworthy,* 1999; *Parsons et al.,* 2001; *Snow & Sutherland*, 2014; *Hizzett et al.,* 2017) have shown that under certain conditions, the rapid sediment loss from surface plumes can generate a secondary turbidity current, which could provide an important mechanism to transport sediment to the depths of the ocean from the continental margin. This is important for interpreting many geological formations, as almost all rivers in the coastal ocean usually have low sediment loads and will almost always form surface plumes rather than plunging hyperpycnal flows (*Mulder & Syvitski,* 1995). As sediment-laden gravity currents are one of the main mechanisms for transport of sediment and their deposition in to lakes and the ocean, we aim to use laboratory experiments in this paper to quantify the conditions that can enhance sedimentation beneath such buoyant sediment-laden river plumes and potentially result in the formation of turbidity currents.

The length-scale over which a surface plume propagates and loses sediment will give a first-order estimate of the scale of sediment deposition from a river mouth, as illustrated schematically in Fig. 1. If there are no currents beneath the surface plume, then the distance at which all of the sediment has fallen out of the plume determines the zone of deposition. This is where the plume stops propagating. The horizontal velocity of the plume (U) is a function its reduced gravity (g'), thickness (H) and Froude number (Fr) as $U = Fr\sqrt{g'H}$, where the

reduced gravity is defined as $g' = g\Delta\rho/\rho$, with g the gravitational acceleration (9.81 m s^{-2}) and $\Delta\rho$ and ρ are respectively the density difference and average density between the current and the saline ambient. The Froude number (Fr) is found to be of order 1 in experimental studies (*Turner,* 1979; *Simpson,* 1982; *Gladstone & Pritchard,* 2010; *Snow & Sutherland,* 2014), and 1 / $\sqrt{2}$ in theoretical studies (*Benjamin,* 1968, *Huppert,* 2006, *Meiburg & Kneller*, 2010). Recent direct numerical simulations of a buoyant double-diffusive gravity currents by *Penney & Stastna* (2016) have suggested that a no-slip condition may increase drag compared to a free-slip condition, and hence would predict different Fr than for regular bottom gravity currents. Hence, the extent of propagation (L_{prop}) can be approximated with equation (1),

$$L_{prop} = U\,T_s = U\,(H/W_s) \quad (1)$$

where U is the plume's horizontal velocity and T_s is the time-scale over which particles settle through the moving surface plume. If the plume has a thickness H, then the time-scale is simply determined as $T_s = H/W_s$, where W_s is the Stokes settling velocity of the sediment particles (*Geyer et al.,* 2004*; Hill et al.,* 2000).

Using typical values for lab and field situations, equation (1) predicts very large propagation length-scales if the only process considered is Stokes settling velocity. For instance a typical gravity current in strongly stratified lab experiments, or in the larger but weakly stratified ocean, usually has a speed of order $U \sim 0.1$ m s^{-1}. The thickness of a typical laboratory gravity current is of order $H = 0.1$ m. Hence, using SiC sediment particles of size 7×10^{-6} m with Stokes settling velocity of $W_s = 7.7 \times 10^{-5}$ m s^{-1}, implies a settling time of $T_s = 1300$ s. Therefore, assuming that our current is moving at 0.1 m s^{-1}, it would need to go a very large distance of 130 m for all the particles to settle out of the plume, and hence laboratory plumes with fine sediment should always propagate to the end of the experimental tanks before losing all of their sediment. Settling velocity in ocean flows on the other hand, will be an order of magnitude slower than for dense SiC particles, and the current's thickness in the range of 1 - 10 m, meaning that length-scales of km would be expected for equation (1). The scaling in equation (1) assumes that within the gravity current particles are settling in a laminar fashion. If the flow is turbulent however, so that the concentration is well mixed, then the average concentration in the flow changes with time as

$C = C_o e^{-t W_s/H}$ (*Martin & Nokes*, 1988; *Sparks et. al*, 1991), so that 95% of particles settle out after 3 settling time-scales, i.e. an even greater distance is implied by equation (1).

There are a number of mechanisms by which the settling velocity in equation (1) could be much faster than the Stokes settling velocity of a single particle, including flocculation and settling-driven convection, both of which would lead to much smaller length-scales of propagation and consequently sedimentation. This study will focus on the potential role of settling-driven convection, as the description of increased settling rates due to flocculation is now quite mature (*Rouhnia & Strom,* 2015, 2017). Field observations have indeed suggested that other processes can enhance the settling of sediment particles over that of the Stokes settling velocity. For instance *Nowacki et al.,* (2012) computed the sediment removal rate from the Colombia River, USA and discovered that the settling rate (10 mm s^{-1}) was substantially larger than the settling velocity of a single particle. Similarly, *Scheu et al.,* (2015) used acoustic backscatter measurements beneath a river plume in a thermally stratified lake, to infer increases of an order of magnitude over the Stokes settling velocities of the suspended sediments settling from turbid river plumes. In the absence of flocculation, the most likely potential mechanism for these increased sedimentation rates is settling-driven convection, the vigor of which depends upon the unstable sediment contrast between the layers.

The process of vigorous settling-driven convection is illustrated in Fig. 2, in which a layer of sediment and fresh water lies above a denser saline layer, where the density difference is due to either temperature and/or salinity. The net density of the sediment-laden layer is lighter than that of the deeper saltier (or colder) layer. Just below the initial interface, downward settling of sediment particles creates a "nose" region, where the material is both salty and sediment-laden and therefore is unstable to convective instabilities. The resulting plumes of sediment-laden material then descends as larger finger-like plumes, which have vertical velocities of at least an order of magnitude faster than the Stokes settling velocities of a single particle. Such finger-like plumes have been seen in a number of studies (*Bradly,* 1965; *Hoyal et al.,* 1999b) and this process is seen to greatly increase the particle removal rate from an otherwise buoyant upper layer (*Houk & Green,* 1973; *Green,* 1987; *Chen,* 1997; *Hoyal et al.,* 1999a, b; *Maxworthy,* 1999; *Parsons & Garcia.* 2000; *Parsons et al.,* 2001; *Davarpanah Jazi & Wells,* 2016). Recent work

by *Davarpanah Jazi & Wells* (2016) found that in a salt/sediment configuration with no horizontal velocity, the vigor of convection was dictated by density ratio defined as $R_\rho = \Delta\rho_S/\Delta\rho_C$, the ratio of density differences due to the added salt and sediment. The most vigorous convection was found to occur for marginal stability when $R_\rho \sim 1$. Theoretical and numerical descriptions of sediment convection (*Burns & Meiburg,* 2012, 2015; *Yu et al.,* 2013, 2014; *Shao et al.,* 2017) have described the timescales for these processes, and revealed the internal dynamics of the velocity fields that are difficult to see experimentally.

One of the key findings of the previous experiments on buoyant plumes is that settling-driven convection is an important mechanism for rapidly moving sediments from the surface to the bed, where they can form a dense turbidity current (*Hoyal et al.,* 1999b; *Maxworthy,* 1999; *Parsons et al.,* 2001). As almost all sediment-laden river plumes are initially buoyant, over a hundred papers have cited *Parsons et al.,* (2001) to suggest settling-driven convection could be a the key process by which turbidity currents can be formed in the coastal ocean near river mouths, which ultimately lead to large sedimentary turbidite structures forming on the ocean floor. However to our knowledge, no actual field studies have specifically studied the process, placing great importance to these earlier experiments. In the current study we aim to revisit these earlier experiments, and improve our understanding on the processes that set the length-scale in equation (1) in light of the improved theoretical understanding of the timescales of settling-driven convection (*Burns & Meiburg,* 2012, 2015*; Yu et al.,* 2013, 2014; *Shao et al.,* 2017). Specifically, our paper aims to quantify the study of *Maxworthy* (1999) by applying the time-scale used in *Burns & Meiburg* (2012, 2015) to determine how the length-scale in equation (1) varies as a function of density ratio (R_ρ).

Our experimental visualizations will shed light on processes occurring underneath buoyant river plumes that are very difficult to observe in the field, but may have a first order effect on the length-scales of current's propagation and depositional sedimentary structures near river mouths. We extend recent theoretical analysis to describe the timescale, over which settling-driven convection occurs, and compare this with a detailed set of visualizations of laboratory experiments. There is good agreement between the theory and the laboratory results, and we

finish the paper with an extrapolation of our findings to river plumes entering lakes and the coastal ocean.

2. MATERIALS AND METHODS

The experiments were performed in a piece of equipment consisting of two compartments that is shown in Fig. 3. It consisted of a rectangular transparent Plexiglas tank with a smaller reservoir separated from the top left corner by a removable metal barrier. These compartments had dimensions of 1.83 × 0.55 × 0.305 m and 0.35 × 0.115 × 0.23 m respectively. To simulate the behavior of a particle-laden flow propagating on top of a lake or the ocean, the isolated section was used to release a fixed volume of sediment and fresh water suspension in to the main compartment containing saline water. Tap water was stored in large buckets overnight to become equilibrated with room temperature (18.5 ± 2.3 ^{o}C) and was used for preparing salt solution and sediment suspension. Thus, temperature was kept constant through all experiments, which resulted in a two-component salt-sediment configuration similar to experiments of *Maxworthy* (1999) and *Hoyal et al.* (1999b).

The sediment used in the experiments was Silicon Carbide (SiC) grinding powder with a density of 3210 kg m^{-3}. It is monodispersed and non-cohesive and previously used in the experiments of *Davarpanah Jazi & Wells* (2016), *Maxworthy* (1999) and *Hoyal et al.* (1999b). With a particle's median diameter and mean Stokes settling velocity of 7.8 × 10^{-6} m and 7.7 × 10^{-5} m s^{-1} respectively, their size distribution was similar to those of *Davarpanah Jazi & Wells* (2016). The ambient saline solution was prepared by dissolving evaporated high purity food grade salt in the stored tap water.

The experiments were characterized based on various density ratios (R_ρ). The density of the ambient was kept constant and different densities of sediment-laden water (ρ_C) were obtained by adding various masses of sediment ($0 \leq m_C \leq 0.065$ kg) to the fixed volume of fresh water within the small compartment. The mass of sediment was determined using an Ohaus SPX222 balance (Ohaus Corporation, Parsippany, NJ, USA) with precision of 10^{-2} g. The densities of saline water (ρ_S) and the compartment, before adding sediment (ρ_{comp}), were measured using an Anton Paar

DMA 35 Ex portable densitometer (Anton Paar USA Inc., Ashland, VA, USA) with an accuracy of ± 10^{-3} g cm^{-3} and a resolution to 10^{-4} g cm^{-3}. The temperatures (t_S, t_{comp}) were measured simultaneously with the same instrument to the precision of 0.2 °C.

The density of a fluid can be determined as $\rho = \rho_0 + \Delta\rho_S + \Delta\rho_C$ and is linearly related to both concentrations of salt and sediment. Here, ρ_0 is the density of clear fresh water at 20°C (998.2 kg m^{-3}), and $\Delta\rho_S$ and $\Delta\rho_C$ are the added density due to the added salt and sediment respectively. The added density due to the added salt was calculated using $\Delta\rho_S = \rho_S - \rho_{comp}$, where ρ_S = 1002.5 ± 0.4 kg m^{-3} and ρ_{comp} = 999.1 ± 0.2 kg m^{-3}. On the other hand, $\Delta\rho_C = \gamma\, C\, \rho_{comp}$ was applied to determine the added density due to the added mass fraction of sediment, in which γ is the density expansion coefficient for SiC particles defined as $(\rho_C - \rho_{comp})/\rho_C$. Furthermore, C is the concentration of sediment particles (kg / kg) denoted by $C = (\frac{m_C}{m_C + m_{comp}})$, where the mass of the compartment (m_{comp}) was determined as $m_{comp} = \rho_{comp}\, V_{comp}$, in which V_{comp} was the volume of the small compartment.

The entire tank was initially filled with saline water with density ρ_S, and then the barrier was inserted to isolate the smaller compartment. With the use of two small pumps, the saline water in this compartment was replaced with freshwater, by discharging salt water out and pumping fresh water in simultaneously. We replaced an equivalent of four times the volume of the small compartment in order to guarantee that 99% of the saline water was flushed out (*Zhixin et al.,* 2014). An electrical mixer was used to keep the fluid well-mixed while being replaced.

The sediment particles were then added to the fresh water in the small compartment and a well-mixed constant volume of sediment-laden water was prepared. The electrical mixer kept the fluid stirred to inhibit the settling of particles and the total time between addition of sediment and removal of barrier was kept to less than two minutes. Each experiment commenced with the gentle removal of the metal barrier 10 s after the mixer was turned off to prevent turbulent motion it produced within the fluid. In addition, food dye was added to the sediment water to further improve flow detection. Digital cameras were used to capture the behavior of the flow from different angles through photos and movies. Two large LED light panels provided bright

and uniform lighting at the background in order to produce clear, sharp photos and movies from the particle-laden gravity current in motion.

A total of 19 experiments with density ratios in the range of $0.687 \leq R_\rho \leq \infty$ were performed. Full details of all 19 experiments, including R_ρ, m_C, L_{prop} and the behavior of sediment laden, are summarized in Table 1. The six supplemental movies are available online and are representative of the major trends in the behavior of the current. In this table the experiments are in an ascending order based on their density ratio. The experiment with $R_\rho = \infty$ had no sediment, and the experiment with $R_\rho = 0.687$ had sediment load such that it was initially denser than saline ambient; all the other 17 experiments were initially positively buoyant and were in the range $1.021 \leq R_\rho \leq 4.575$. The above two experiments ($R_\rho = \infty$ and 0.687) were performed only for comparison purposes, but the main focus of our study was on particle-laden overflows. We measured the propagation length-scale of the gravity current (L_{prop}) by visually determining the distance at which the thickness of the gravity current became less than 0.01 m.

2.1. Theory

We expect that the propagation length-scale of the gravity current L_{prop} will be reduced by the influence of settling-driven convection, compared to the simple estimate we made in equation (1), where only Stokes settling velocities are important. We will now modify the scaling of L_{prop} to take into account theoretical scaling of the sedimentation timescale, introduced by *Burns & Meiburg* (2012, 2015) to show how the density ratio R_ρ and the stratification influence the propagation length-scale. The horizontal plume velocity is a function of the reduced gravity, which can be expressed in terms of the contribution of sediment and salt density anomalies as,

$$U = Fr \sqrt{\frac{g\,H}{\rho}(-\Delta\rho_C + \Delta\rho_S)} \qquad (2)$$

where $\Delta\rho_S$ and $\Delta\rho_C$ are the added density due to the added salt and mass fraction of sediment respectively. If we introduce the definition of density ratio ($R_\rho = \Delta\rho_S/\Delta\rho_C$) previously used by *Davarpanah Jazi & Wells* (2016), then this velocity can be rewritten in terms of R_ρ as,

$$U = Fr\sqrt{\frac{g\ \Delta\rho_S}{\rho}H\left(1 - \frac{1}{R_\rho}\right)} \tag{3}$$

The propagation length-scale of sediment beneath a gravity current (L_{prop}), as mentioned earlier in equation (1), is a function of its velocity (U) and sedimentation time-scale (T_s). The settling-driven convection instability is driven by the downward settling of sediment from the fresher layer to the denser saline layer (Figs. 2b and 2C). A very thin layer of fluid, just below the interface containing both salt and sediment, forms a "nose" of unstable stratification of length-scale (l). The so-called unstable nose region (*Burns & Meiburg,* 2012) can become gravitationally unstable over time due to the accumulation of particles and grows until the Grashof number is of order unity (*Hoyal et al.,* 1999b), at which stage the layer will sink as a convective plume. The Grashof number is defined as,

$$Gr = g'_C\, l^3/\nu \tag{4}$$

where $g'_C = \frac{g\ \Delta\rho_C}{\rho_0}$ is the reduced gravity defined in terms of the density difference due to the added sediment ($\Delta\rho_C$) and density of fresh water (ρ_0) (*Burns & Meiburg,* 2012) and ν is the kinematic viscosity of fresh water at 20 ^{o}C (10^{-6} m^2 s^{-1}). With this interface, we can also define a Reynolds number as,

$$Re = w_s l/\nu \tag{5}$$

If we then assume that in the nose region $Re = Gr = 1$, *Burns & Meiburg* (2012) showed that the only time-scale emerging is defined as,

$$T_S \sim \left(\frac{\nu}{g'^2_C}\right)^{1/3} \tag{6}$$

In the numerical simulations of *Burns & Meiburg* (2012, 2015) and *Shao et al.* (2017), the time is non-dimensionalzed by equation (6) and their resulting 3D simulations suggest that it takes of order 100 time-scales for fully developed sedimentary convection to develop. We will refer to C_T as the dimensionless multiple of the time in equation (6) that it takes for sedimentary convection to develop, and will determine the value of C_T experimentally. Assuming that the sedimentary convective time-scale of *Burns & Meiburg* (2012) is the relevant time-scale for sediment to be lost from the sharp density interface beneath the overflow, then we can combine equations (3) and (6) to estimate a propagation length-scale (L_{prop}) for the gravity current as,

$$L_{prop} \sim Fr \sqrt{g \frac{\Delta\rho_S}{\rho_0} H \left(1 - \frac{1}{R_\rho}\right)} \; \nu^{1/3} \left(g \frac{\Delta\rho_C}{\rho_0}\right)^{-2/3} \tag{7}$$

To see the dependence upon R_ρ even more clearly, by keeping the salinity anomaly $\Delta\rho_S$ constant and assuming $Fr \sim 1$, we then introduce two dimensional constants, $C_1 = \sqrt{g \frac{\Delta\rho_S}{\rho_0} H}$ and $C_2 = \nu^{1/3} \left(g \frac{\Delta\rho_S}{\rho_0}\right)^{-2/3}$, with units of m s^{-1} (speed) and s (time) respectively. This reduces the propagation length-scale to a simple function of R_ρ as,

$$L_{prop} = C_1 C_2 C_T \sqrt{\left(1 - \frac{1}{R_\rho}\right)} R_\rho^{2/3} \tag{8}$$

where the combined coefficients $C_1 C_2$ (assuming $\rho \approx \rho_0$) can be furthermore simplified to provide a scale constant (with units of m) as,

$$C_1 C_2 = \sqrt{H} \; \nu^{1/3} \left(g \frac{\Delta\rho_S}{\rho}\right)^{-1/6} \tag{9}$$

The propagation length-scale (L_{prop}) in equation (8) goes to zero as R_ρ approaches unity (when there is no density difference between the two layers) and it increases as $R_\rho^{\,2/3}$ for large R_ρ.

3. RESULTS

The vigor of convection strongly increases with the decrease of R_ρ towards unity, and striking differences in the behavior of the sediment laden current can be seen. In particular, the propagation length-scale of the plume is a strong function of the density ratio and decreases as R_ρ gets close to one.

The vigor and form of sediment convection changes dramatically with the change in R_ρ (Fig. 4). The series of photographs in Fig. 4 depicts the behavior of the flow every 30 s for R_ρ = 3.051 and 1.48 (left and right panels respectively). The behaviors seen for R_ρ = 3.051 in Figs. 4 a to 4 j was a result of weak settling-driven convection. *Davarpanah Jazi & Wells* (2016) had similar observations of settling-driven convection shown schematically in their Fig. 1 b. On the other hand for a smaller density ratio of R_ρ = 1.48, Figs. 4 k to 4 t depicts a very vigorous mode of settling-driven convection, which resulted in the rapid sinking of distinct finger-like structures. The estimated time from the Stoke settling velocity for a single SiC particle to go from the top to the bottom of our experiment tank is 2 hr. However, Figs. 4 j and 4 q display evidence of settling to the bottom after 270 s and 180 s respectively. This shows that settling-driven convection has a substantial effect on increasing the downward velocity of collections of SiC particles. In addition, this Fig. clearly displays the difference in vertical settling velocities for high and low density ratios. In Fig. 4 g, corresponding to R_ρ = 3.051, small plumes of sediment descend very slowly 180 s after pulling the barrier, whereas in Fig. 4 q, corresponding to R_ρ = 1.48, large fingers of sediment have travelled more than 40 cm of tank's height and are close the bottom boundary.

The differences in the shapes formed by the convection with the change in R_ρ are better observed in the close up images that illustrate the shift in features such as width and velocity of the convective sediment fingers (Fig. 5). Fig. 5 displays zoomed in photos, taken every 30 s, of weaker settling-driven convection for R_ρ = 4.575 and a much more vigorous settling-driven convection for R_ρ = 1.229. The times on these set of photos again indicate faster velocities in the latter situation, where the fingers of sediment were wider and grew larger in size well before the

current reached the end wall. The vertical velocity of the small plumes and the large fingers can be estimated as 0.06 cm s^{-1} and 0.3 cm s^{-1} respectively. As a general trend in Figs. 4 and 5 it can be concluded that with the decrease in R_ρ towards unity, the current moved slower horizontally and the formation of finger-like structures occurred earlier. Therefore, the propagation speed and length of the current diminished. With the increase in the mass of particles for lower R_ρ, the sediment settled out of current faster as well as entraining water out of the current. Therefore, the head of the current decreased in size and could eventually stop before the end of the tank if convection was vigorous enough.

In many experiments where strong sediment convection occurred, either a turbid interflow or an intense turbidity current at the base of the tank was formed (Fig. 6). The series of photos in Fig. 6, taken every 60 s, displays these two distinct behaviors of flow for R_ρ = 1.172 and R_ρ = 1.054. In both cases the current moved visibly slower than those discussed earlier in Fig. 5. As can be seen in Fig. 6, both currents never reached the end of the tank and stopped before reaching the 1.5 m, as the sediments settled rapidly due to the very vigorous settling-driven convection of SiC particles. In Figs. 6 e to 6 j, corresponding to R_ρ = 1.172, after the overflow stopped at L_{prop} = 1.3 m, it was interesting to observe the emergence of an interflow below the initial overflow, which lasted for a long time. In this case not only the sediment particles were falling down but they were also dragging water down with them. However, these plumes were not heavy enough to plunge down to the bottom of the tank. Therefore, the amount of water that the plume carried with itself became important (similar observations are reported in *Sutherland et al.* (2018)). On the other hand, for R_ρ = 1.054 the overflow stopped at a shorter distance of L_{prop} = 0.75 m and an underflow occurred shortly after. This behavior was quite similar to observations made by *Maxworthy* (1999).

The difference in horizontal velocities of the descending plumes with various density ratios can be easily seen by putting together horizontal time slices of photos taken from the top 0.127 m of the overflow as displayed in Fig. 7. Three cases of R_ρ = ∞, 2.492 and 1.172 are considered here. The speed of the overflow was determined by fitting the best line to the front of the current in each stack of images. The speeds corresponding to the density ratios under consideration were

$U_{R_\rho=\infty}$ = 0.0279 m s^{-1}, $U_{R_\rho=2.492}$ = 0.0246 m s^{-1} and $U_{R_\rho=1.172}$ = 0.0068 m s^{-1}. Note that for R_ρ = 1.172 the gravity current stops at L_{prop} =1.3 m as was also displayed in Fig. 6. The comparison of the initial speed of the propagating overflow in the three Figs. shows a faster speed for the larger density ratios, consistent with the scaling of equation (3) that $U \sim \sqrt{\left(1 - \frac{1}{R_\rho}\right)}$. This equation determines the Froude number for $R_\rho = \infty$ to be $Fr_{R_\rho=\infty}$ = 0.820 based on the experimental speed. Furthermore, estimations of the Froude number based on equation (3) for R_ρ = 2.492 and 1.172 are $Fr_{R_\rho=2.492}$ = 0.880 and $Fr_{R_\rho=1.172}$ = 0.506 respectively, smaller than some previous estimates of gravity currents without sedimentary convection.

There is good agreement between the theoretical prediction of equation (8) and experimental results of the propagation length-scale of the gravity current as a function of various density ratios (Fig. 8). As can be seen with the decrease in R_ρ the propagation length-scale tends to shorten. The data points are surrounded by two curves in blue, which provided upper and lower bounds on the constants C_1C_2 in equation (9). For our experimental conditions, where 2.9 kg m^{-3} $\leq \Delta\rho_S \leq$ 3.7 kg m^{-3}, the two constants are in the range of 0.0380 $\leq C_1 \leq$ 0.0619 m s^{-1}and 0.0967 $\leq C_2 \leq$ 0.1848 s, so that $C_{1avg}C_{2avg}$ = 0.0069 m. As outlined earlier, previous numerical simulations of *Burns & Meiburg* (2012, 2015) suggest that it will take several hundred timescales for large "finger" instabilities to develop, and so in Fig. 8 we plot the blue theoretical curves to have values of 390 and 550. These two values bracket the observations well and are consistent with our expectation that C_T is of order 100. For typical values of C_1 and C_2 in lab conditions, with 1 < R_ρ < 2, we predict the propagation length-scale to be 0 < $L_{prop} \leq$ 1.83 m. Furthermore, for any R_ρ > 1.3 in our experiments the observed propagation length-scale (L_{prop}) was limited to the tank length of 1.83 m. We note that all these observations has length-scales dramatically smaller than the prediction of L_{prop} based upon the particle settling rate in equation (1), which is a direct result of the increase in falling of particles under the influence of settling-driven convection process.

4. DISCUSSION

There is a striking influence of the density ratio upon the fate of suspended sediments from a buoyant river plume and Fig. 9 summarizes the general flow behaviors observed in all of our experiments. For R_ρ > 2, we observed weak settling-driven convection and slow sinking of particles in experiments that lasted for long duration of time. On the other hand, when 1.3 < R_ρ < 2 fingers of sediment were rapidly sinking under the direct effect of strong and vigorous settling-driven convection. In both of the above mentioned cases the current reached the end wall. However, in the latter it was moving visibly slower as it lost particles over time and its driving force diminished. When 1.17 < R_ρ < 1.23, the motion of the current was even slower to the point that it stopped before reaching the end wall and an interflow occurred afterwards. Finally, for cases where R_ρ was very close to unity not only the surface flow stopped, but also an intense underflow was observed. We note that the bounds in Fig. 9 are specific to the length of our tank. For instance, if our tank had been 10 m, it is likely that all the flows would have stopped, and hence formed some sort of subsurface gravity current. We furthermore note that it is possible that the geometry of tank's bottom may also be an important aspect. The experimental setup in both of the studies made by *Parsons et al*. (2001) and *Snow & Sutherland* (2014) included a sloping ramp, which would probably increase the tendency to form turbidity currents beneath an overflow.

One of the most interesting results of our experiments is that we have quantified the scale over which it is likely that a surface sediment-laden plume can transform into a subsurface turbidity current (Fig. 10). In lakes with smaller lengths than L_{prop} we expect sediment to rain down uniformly over the lake bed, but if L_{prop} is sufficiently small, then a turbidity current could form. This mechanism of turbidity current formation was first expressed by *Maxworthy* (1999) and greatly popularized in the sedimentology literature by *Parsons et al*. (2001). It is often invoked as a potential mechanism by which turbidity currents can form, with the note that typically sediment loads in rivers are not high enough to directly form hyperpycnal flows (*Mulder & Syvitski,* 1995; *Mulder & Chapron,* 2011). The overflow enters the lake and propagates until enough particles have settled out where it stops at the distance L_{prop}, and continue as an underflow (and in some cases as an interflow). There are various parameters that can influence its behavior such as density ratio (R_ρ), density of the ambient (ρ_S), temperature (t_S, t_{comp}), the slope of the tank's bottom boundary, strong stratification and particle size.

Having no slope in the tank's bottom or strong stratification, by keeping the temperature and the ambient density constant in the current study, we specifically show that varying R_ρ can have an important effect on the fate of a particle-laden overflow due the strong and vigorous settling-driven convection of sediment particles. Our experimental observations and theoretical predictions confirm that the propagation length-scale of such a flow can dramatically change once R_ρ gets very close to unity and it scales as $L_{prop} \sim \sqrt{1 - 1/R_\rho}\, R_\rho^{2/3}$.

We expect that sediment-laden river inflows into lakes will typically have much lower R_ρ than in the coastal ocean, so that the behavior of sedimentation and deposition scales will be very different for the same sediment load in a river (Fig. 9). When a river flows into a lake, the density difference arises due to the temperature anomaly (rather than the salinity difference). The largest density anomaly we might expect would be a 20 °C river flowing into a 10 °C lake, so that $g\,\Delta\rho_S/\rho$ = 0.0146 m s^{-2}. In contrast, for a fresh river entering the ocean saline water the reduced gravity would be of order $g\,\Delta\rho_S/\rho$ = 0.294 m s^{-2}, i.e. at least 20 times greater. Thus, for the same sediment load R_ρ is always much larger than 1 in the ocean than in a lake. Underflows are frequently observed in rivers entering lakes (see for example Fig. 19 D-2 in *Talling et al.* (2013) and *Cossu et al.* (2015)), whereas only very rarely do rivers have enough sediment load in the ocean to form underflow (*Mulder & Syvitski,* 1995; *Mulder & Chapron,* 2011). As an example, *Hizzett et al.* (2017) describe sediment concentrations as usually being less than 0.07 kg m^{-3} in Squamish River. In the coastal ocean this is clearly insufficient to form an underflow directly, and we would estimate R_ρ ~ 25 kg m^{-3} / 0.07 kg m^{-3} ~ 350. In contrast, if this same river flowed into a thermally stratified lake with a large 10 ^{o}C difference across the thermocline, it would have R_ρ ~ 1.5 kg m^{-3} / 0.07 kg m^{-3} ~ 20, and could potentially even have R_ρ ~ 1, if the temperature difference between river and lake was less than 1 ^{o}C. For R_ρ >> 1 then $L_{prop} \sim R_\rho^{2/3}$, so the difference in propagation length between R_ρ = 20 and 350 is a factor of 100, indicating a substantial difference in the likely deposition behavior between a lake and the ocean.

While the density ratio is the most important parameter in determining the various behaviors described in Fig. 9, we also need to discuss how the coefficients in equation (9) vary with the

current's thickness, and the salinity difference, in order to extrapolate from the laboratory experiments to field situations. There is only a very weak dependence upon $\Delta\rho_S$ in equation (10), so that the main control on the constants (C_1C_2) is the change in thickness of the current H, which will vary by an order of 1-2 between lab and field experiments. To show this weak dependence quantitatively, for example in the ocean as the salinity is very high, the density difference would arise due to the added salt (and not difference in temperature). As the coefficient in (9) scales $\Delta\rho_s^{-1/6}$, while there is an order of magnitude difference in reduced gravity between the ocean and lake case, the ratio of these terms is $(0.294 / 0.0146)^{-1/6} = 0.6$, i.e. a very small difference. In contrast, in equation (9) there is a much stronger dependence on depth, as $C_1C_2 \sim \sqrt{H}$. Therefore, as typical laboratory plume thicknesses are of order 0.1 m and river plumes thicknesses are of order 10 m, this change in scale leads to a factor of 10 times greater range for deposition. We furthermore believe that particle size will likely affect the current's propagation (*Sutherland et al.,* 2018) in the sense that larger particles tend to settle faster and hence diminish L_{prop}. While some numerical work (i.e., *Burns & Meiburg,* 2012, 2015; *Yu et al.,* 2014, 2015) and experimental studies (*Sutherland et al.,* 2018) has suggested a weak dependence of the vigor of convective sedimentation (settling-driven convection) upon particle size, this remains an important area of future work.

As far as we are aware, there are no direct field observations of the process of settling-driven convection, hence our videos of the various experiments provide a useful guidance for the expected behavior (Supplementary material) and the possible design of future field observation campaigns. The idea from *Parsons et al*. (2001) that convective sedimentation (settling-driven convection) can lead to formation of turbidity currents has been often invoked to explain field observations of turbidity currents, but only a few field studies detail some of the causal links. For instance, *Hizzett et al.* (2017) noted that the occurrence of turbidity current below the delta of the Squamish River correlated best with the presence of sediment-laden river plumes, rather than slope failures on the delta. In addition, *Schue et al.* (2015) studied a sediment laden river plume flowing into a thermally stratified Alpine lake, and observed (using acoustic backscatter) that the vertical velocity of a descending sediment layer below a river plume was an order of magnitude greater than Stokes settling velocities, consistent with our experimental plumes in Fig. 4. *Petticrew et al.* (2015) also conducted a study on a mine disaster in the Mount Polley at Quesnel

Lake in BC, Canada (Aug 4th 2014), where a large volume of mining tailings entered a stratified water body and formed a persistent 20 m thick turbid layer below the thermocline. Their data suggested that a water column with density difference of 0.07 kg m^{-3} and ~ 2.5 ^{o}C temperature increase (5 ^{o}C to ~ 7.5 ^{o}C) remained suspended 30m below the surface, which didn't rise to the surface despite being warm. This water was transported as a plume held below the thermocline at the speed of ~ 0.1 m s^{-1} (*Petticrew et al.,* 2015). Furthermore, *Giovanoli* (1990) studied the transport of sediments from Rhône River flowing into Lake Geneva as an interflow. As mentioned in this study, the sediment concentration in the river is in the range of 10 – 5000 mg l^{-1}. With the assumption that there is a 10 ^{o}C temperature difference between the two layers, it would result in a density ratio within the range of $0.3 < R_\rho < 150$ (R_ρ ~ 1.5 kg m^{-3} / 5 kg m^{-3} ~ 0.3 and R_ρ ~ 1.5 kg m^{-3} / 0.01 kg m^{-3} ~ 150).

The depth of neutral buoyancy is where the density difference between the layers are minimal, i.e. R_ρ ~ 1, and an interflow can form. *Davarpanah Jazi & Wells* (2016) concluded that large turbulent velocities and strong convection at this depth results in the accumulation of sediment particles closer to the mouth of the rivers. Moreover, they define double-diffusive convection as the dominant sedimentation process for R_ρ close to unity based on their regime diagram. The current study redefines their criteria in a new level by the fact that double-diffusive convection dominates at a very small time scale and infinitely marginal density differences of the two layers. Our new observations shows that the defined criteria under the effect of settling-driven convection by *Davarpanah Jazi & Wells* (2016), $1.2 < R_\rho \leq 18.06$ can now be redefined based on Fig. 9. We would recommend in future field work, that the sediment concentration be monitored in the river, and the salinity or temperature contrast be measured, so that R_ρ could be estimated. Furthermore, an upwards looking ADCP could determine the vigour of any sedimentation plumes, and a downward looking ADCP could determine if any turbidity currents result. Such a field campaign could then determine the degree to which the ideas presented by *Parsons et al*. (2001) are valid for the formation of turbidity current, compared to other processes such as flocculation.

A final area where the dynamics of settling driven convection is relevant is in the dynamics of pyroclastic flows, especially how the hot volcanic ash cloud might intrude into the thermally

stratified atmosphere. Indeed our work is related to previous experiments of *Carazzo & Jellinek* (2012, 2013), *Manzella et al.* (2015) and *Scollo et al.* (2017), who studied the dynamics of sedimentary convection in order to interpret field observations of ash laden volcanic clouds. In particular, geologists often wish to know the radius over which ash will deposit, as this has important hazard prediction implications. Our video imagery might further help interpret these field observations.

REFERENCES

Benjamin, T. B. (1968) Gravity currents and related phenomena. *J. Fluid Mech*., **31**, 209 – 248.

Bonnecaze, R. T., Huppert, H. E. and **Lister, J. R.** (1993) Particle-driven gravity currents. *J. Fluid Mech.*, **250**, 339 – 369.

Bradley, W. H. (1965) Vertical density currents. *Science*, **150** (3702), 1423 – 1428.

Burns, P. and **Meiburg, E.** (2012) Sediment-laden fresh water above salt water: Linear stability analysis. *J. Fluid Mech.*, **691**, 279 – 314.

Burns, P. and **Meiburg, E.** (2015) Sediment-laden fresh water above salt water: Nonlinear stability analysis. *J. Fluid Mech.*, **762**, 156 – 195.

Carazzo, G. and **Jellinek, A. M.** (2012) A new view of the dynamics, stability and longevity of volcanic clouds. *Earth Planet. Sci. Lett.*, **325 – 326**, 39 – 51.

Carazzo, G. and **Jellinek, A. M.** (2013) Particle sedimentation and diffusive convection in volcanic ash-clouds. *J. Geophys. Res. Solid Earth*, **18**, 1420 – 1437, doi:10.1002/jgrb.50155.

Chen, C. F. (1997) Particle flux through sediment fingers. *Deep Sea Res.*, **44** (9 – 10), 1645 – 1654.

Cossu, R., Forrest A. L., Roop, H. A., Dunbar, G. B., Vandergoes, M. J., Levy, R. H., Stumoner, P. and **Schladow, S. G.** (2015) Seasonal variability in turbidity currents in Lake Ohau, New Zealand, and their influence on sedimentation. *Mar. Freshwater Res.*, doi:10.1071/MF15043.

Davarpanah Jazi, S. and **Wells, M.G.** (2016) Enhanced sedimentation beneath particle□laden flows in lakes and the ocean due to double□diffusive convection. *Geophys. Res. Lett.*, **43** (20), 10883 – 10890, doi: 10.1002/2016GL069547.

Geyer, W. R., Hill, P. S. and **Kineke, G. C.** (2004) The transport, transformation and dispersal of sediment by buoyant coastal flows. *Cont. Shelf Res.*, **1212** (24), 927 – 949.

Giovanoli, F. (1990) Horizontal transport and sedimentation by interflows and turbidity currents in Lake Geneva. In *Large Lakes*, edited by Tilzer, M. M. and Serruya, C., pp. 175 – 195, Springer, Berlin.

Gladstone, C. and **Pritchard, D.** (2010) Patterns of deposition from experimental turbidity currents with reversing buoyancy. *Sedimentology*, **57**, 53 – 84.

Green, T. (1987) The importance of double diffusion to the settling of suspended material. *Sedimentology*, **34**, 319 – 331.

Hill, P. S., Milligan, T. G. and **Geyer, W. R.** (2000) Controls on effective settling 1216 velocity of suspended sediment in the Eel River flood plume, *Cont. Shelf Res.*, **20** (16), 2095 – 2111.

Hizzett, J. L., Hughes Clarke, J. E., Sumner, E. J., Cartigny, M. J. B., Talling, P. J. and **Clare, M. A.** (2017) Which triggers produce the most erosive, frequent and longest runout turbidity currents on deltas? *Geophys. Res. Lett.*, **45**, doi: 10.1002/2017GL075751.

Horner-Devine, A. R., Hetland, R. D. and **MacDonald, D. G.** (2015) Mixing and transport in coastal river plumes. *Annu. Rev. Fluid Mech.*, **47**, 569 – 594.

Houk, D. and **Green, T.** (1973) Descent rates of suspension fingers. *Deep Sea Res.*, **20**, 757 – 761.

Hoyal, D. C. J. D., Bursik, M. I. and **Atkinson, J. F.** (1999a) The influence of diffusive convection on sedimentation from buoyant plumes. *Mar. Geol.*, **159**, 205 – 220.

Hoyal, D. C. J. D., Bursik, M. I. and **Atkinson, J. F.** (1999b) Settling-driven convection: A mechanism of sedimentation from stratified fluids. *J. Geophys. Res.*, **104** (C4), 7953 – 7966, doi: 10.1029/1998JC900065.

Huppert, H. E. (2006) Gravity currents: a personal perspective. *J. Fluid Mech.*, **554**, 299 – 322.

Manzella, I., Bonadonna, C., Phillips, J. C. and **Monnard, H.** (2015) The role of gravitational instabilities in deposition of volcanic ash. *Geology*, **43** (3), 211 – 214.

Martin, D. and **Nokes, r.** (1998) Crystal settling in a vigorously convecting magma chamber. *Nature*, **332**,534 – 536.

Maxworthy, T. (1999) The dynamics of sedimenting surface gravity currents. *J. Fluid Mech.*, **392**, 27 – 44.

Meiburg, E. and **Kneller, B. C.** (2010) Turbidity currents and their deposits. *Annu. Rev. Fluid Mech.*, **42**, 135 – 156.

Mulder, T. and **Chapron, E.** (2011) Flood deposits in continental and marine environments: character and significance. In *Sediment Transport from Shelf to Deep Water — Revisiting the Delivery System*, AAPG Stud. Geol., vol. **61**, edited by R. M. Slatt and C. Zavala, pp. 1 – 30.

Mulder, T. and **Syvitski, J. P. M.** (1995) Turbidity currents generated at river mouths during exceptional discharges to the world oceans. *J. Geol.*, **103** (3), 285 – 299.

Nowacki, D. J., Horner-Devine, A. R., Nash, J. D. and **Jaym, D. A.** (2012) Rapid sediment removal from the Columbia River plume nearfield. *Cont. Shelf Res.* **35**, 16 – 28.

Parsons, J. D. and **Garcia, M. H.** (2000) Enhanced sediment scavenging due to double-diffusive convection. *J. Sediment. Res.*, **70** (1), 47 – 52.

Parsons, J. D., Bush, J. W. M. and **Syvitski, J. P. M.** (2001) Hyperpycnal plume formation from riverine outflows with small sediment concentrations. *Sedimentology*, **48** (2), 465 – 478.

Penney, J. and **Stastna, M.** (2016) Direct numerical simulation of double-diffusive gravity currents. Physics of Fluids **28**, 086602; doi: 10.1063/1.4961045.

Petticrew, E. L., Albers, S. J., Baldwin, S. A., Carmack, E. C., Déry, S. J., Gantner, N., Graves, K. E., Laval, B., Morrison, J., Owens, P. N., Selbie, D. T. and **Vagle, S.** (2015) The impact of a catastrophic mine tailings impoundment spill into one of North America's largest fjord lakes: Quesnel Lake, British Columbia, Canada. *Geophys. Res. Lett.*, **42**, 3347–3355, doi: 10.1002/2015GL063345.

Rouhnia, M. and **Strom, K.** (2015) Sedimentation from flocculated suspensions in the presence of settling-driven gravitational interface instabilities. *J. Geophys. Res. Oceans*, **120**, 6384 – 6404, doi: 10.1002/2015JC010750.

Rouhnia, M. and **Strom, K.** (2017) Sedimentation from buoyant muddy plumes in the presence of interface mixing: an experimental study. *J. Geophys. Res. Oceans*, **120**, 2652 – 2670, doi: 10.1002/2016JC012053.

Shao, Y. C., Hung, C. Y. and **Chou, Y. J.** (2017) Numerical study of convective sedimentation through a sharp density interface. *J. Fluid Mech.,* **824**, 513 - 549.

Scheu, K. R., Fong, D. A., Monismith, S. G. and **Fringer, O. B.** (2015) Sediment transport dynamics near a river inflow in a large alpine lake. *Limnol. Oceanogr.*, **60** (4), 1195 – 1211.

Simpson, J. E. (1982) Gravity currents in the laboratory, atmosphere and ocean. *Ann. Rev. Fluid Mech.*, **14** (1), 213 – 234.

Snow, K. and **Sutherland, B. R.** (2014) Particle-laden flow down a slope in uniform stratification. *J. Fluid Mech.*, **755**, 251 – 273.

Scollo, S., Bonadonna, C., and **Manzella, I.** (2017) Settling-driven gravitational instabilities associated with volcanic clouds: new insights from experimental investigations. *Bulletin of Volcanology*, **79**:39. https://doi.org/10.1007/s00445-017-1124-x.

Sparks, R. S. J., Carey, S. N. and **Sigurdsson, H.** (1991). Sedimentation from gravity currents generated by turbulent plumes. *Sedimentology*, **38** (5), 839 - 856.

Sutherland, B. R., Gingras, M. K., Knudson, C., Steverango, L. and **Surma, C.** (2018) Particle-bearing currents in uniform density and two-layer fluids. *Phy. Rev. Fluids*, in press.

Talling, P. J., Paull, C. K. and **Piper, D. J. W.** (2013) How are subaqueous sediment density flows triggered, what is their internal structure and how does it evolve? Direct observations from monitoring of active flows. *Earth-Sci. Rev.*, **112**, 244 - 288.

Turner, J. S. (1979) Buoyancy Effects in Fluids. Cambridge University Press.

Warrick, J. A., Xu, J., Marlene, A. N. and **Homa, J. L.** (2008) Rapid formation of hyperpycnal sediment gravity currents offshore of a semi-arid California river. *Cont. Shelf Res.*, **28**, 991 – 1009.

Yuan, Y. and **Horner-Devine, A.R.** (2017) Experimental investigation of large-scale vortices in a freely spreading gravity current. *Phys. Fluids*, 29(10), p.106603. https://doi.org/10.1063/1.5006176.

Yu, X., Hsu, T. J. and **Balachandar, S.** (2013) Convective instability in sedimentation: Linear stability analysis. *J. Geophys. Res. Oceans*, **118**, 256 – 272, doi:10.1029/2012JC008255.

Yu, X., Hsu, T. J. and **Balachandar, S.** (2014) Convective instability in sedimentation: 3-D numerical study. *J. Geophys. Res. Oceans*, **119**, 8141 – 8161, doi:10.1002/2014JC010123.

Zhixin, Q., Eames, I. and **Greig, A.** (2014) Flushing ballast tanks. *Ocean Eng.*, **89**, 157 – 172.

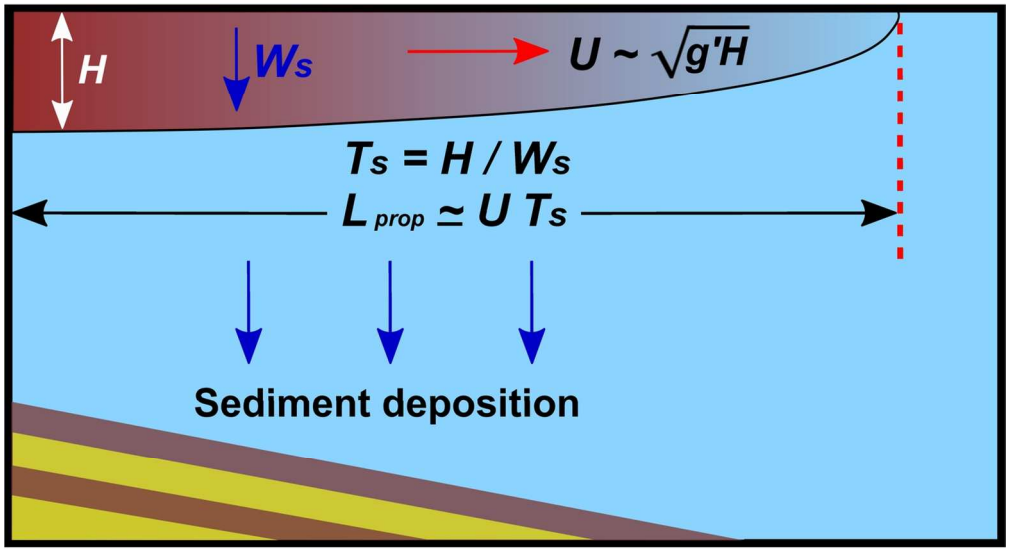

Fig. 1: Conceptual diagram of the relevant scales beneath a buoyant sediment-laden current.

137x74mm (300 x 300 DPI)

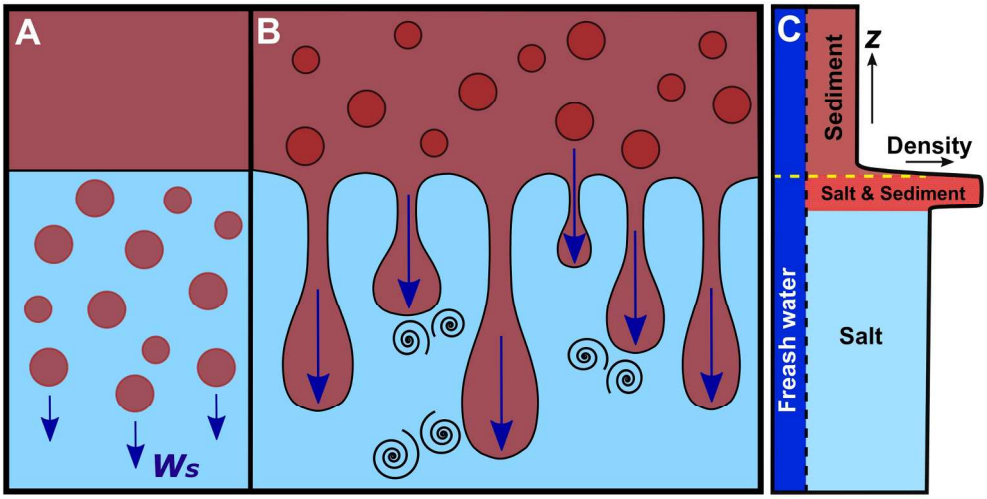

Fig. 2: Schematic of (A) Stokes settling of individual particles, (B) the vigorous settling-driven convection of sediment particles and (C) the unstable nose region containing both salt and sediment.

210x149mm (300 x 300 DPI)

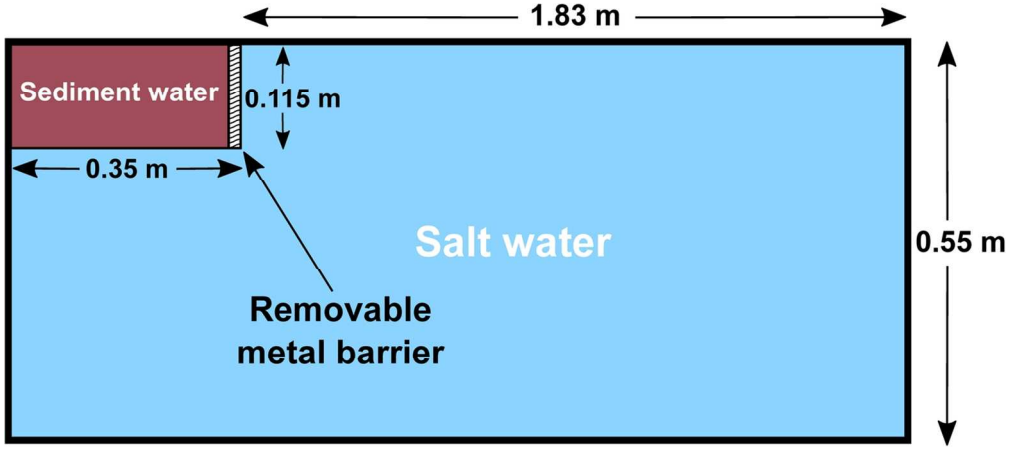

Fig. 3: Schematic side view of the experimental setup, showing the main tank, isolated compartment and removable metal barrier.

128x56mm (300 x 300 DPI)

Table 1: The data corresponding to the conducted experiments.

Exp. No.	R_ρ	$t_s\ (°C)$	$t_{comp}\ (°C)$	$m_C\ (kg)$	$L_{prop}\ (m)$	Flow behavior
1	0.687	16.8	16.2	0.065	-	Strong underflow / Movie S1
2	1.021	18.2	18.2	0.045	0.65	Fig. 9D
3	1.054	18.7	18.8	0.041	0.75	Fig. 9D / Movie S2
4	1.093	19.9	20.1	0.042	1	Fig. 9D
5	1.107	20.7	20.4	0.039	1.1	Fig. 9D
6	1.151	21	20.8	0.034	1.25	Fig. 9D
7	1.172	20.6	20.5	0.038	1.3	Fig. 9C
8	1.230	20.8	20.4	0.034	1.55	Very weak version of Fig. 9D
9	1.233	20.5	20.3	0.035	1.6	Fig. 9C
10	1.308	21	20.6	0.033	1.83	Fig. 9B
11	1.391	20.6	20.6	0.032	1.83	Fig. 9B / Movie S3
12	1.433	18.7	18.8	0.032	1.83	Fig. 9B / Movie S4
13	1.483	20.6	20.5	0.030	1.83	Fig. 9B
14	1.779	20.6	20.6	0.025	1.83	Fig. 9B
15	2.155	20.1	19.9	0.020	1.83	Weak version of Fig. 9B
16	2.492	17.4	19.3	0.020	1.83	Fig. 9A
17	3.051	19.8	19.7	0.015	1.83	Fig. 9A
18	4.575	18.5	18.7	0.010	1.83	Fig. 9A / Movie S5
19	∞	19.7	20.2	0	1.83	Strong overflow / Movie S6

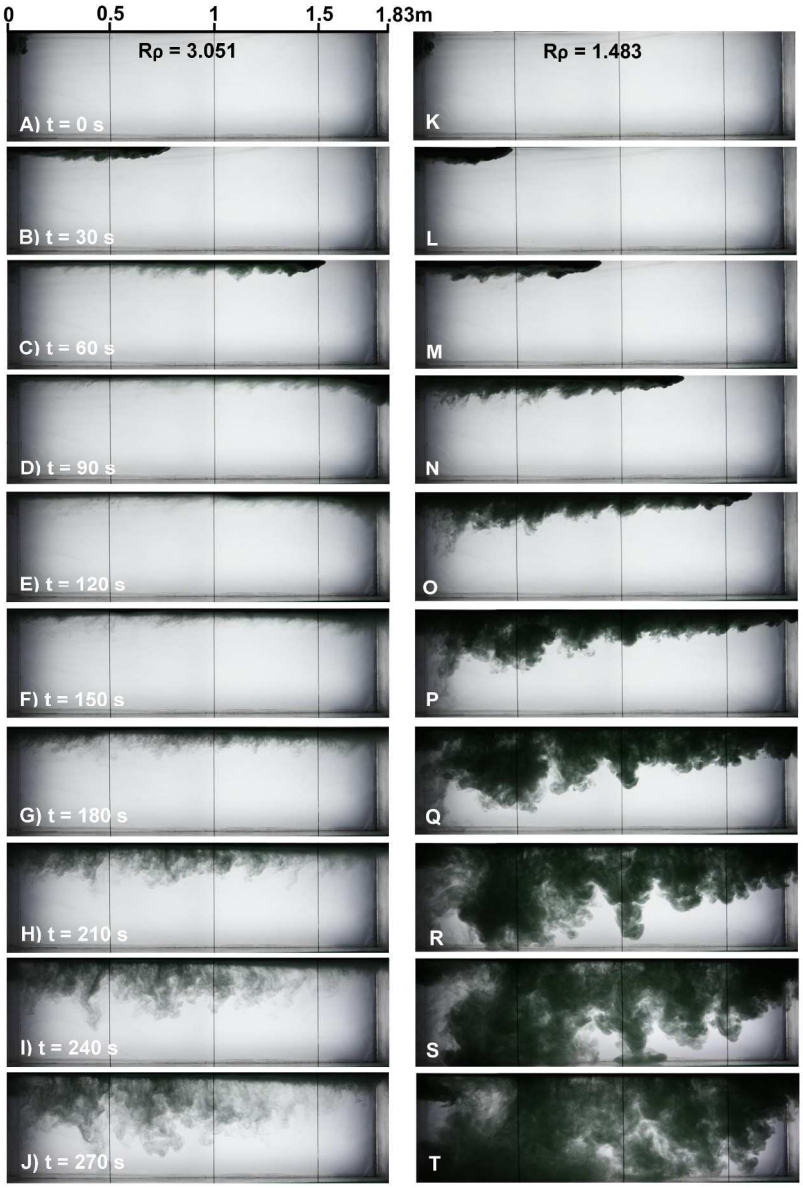

Fig. 4: Photos of experiments showing (A) to (J) weak settling-driven convection and (K) to (T) vigorous settling-driven convection. Two set of photos showing difference in vertical settling velocities for R_ρ = 3.051 and R_ρ = 1.483.

251x359mm (300 x 300 DPI)

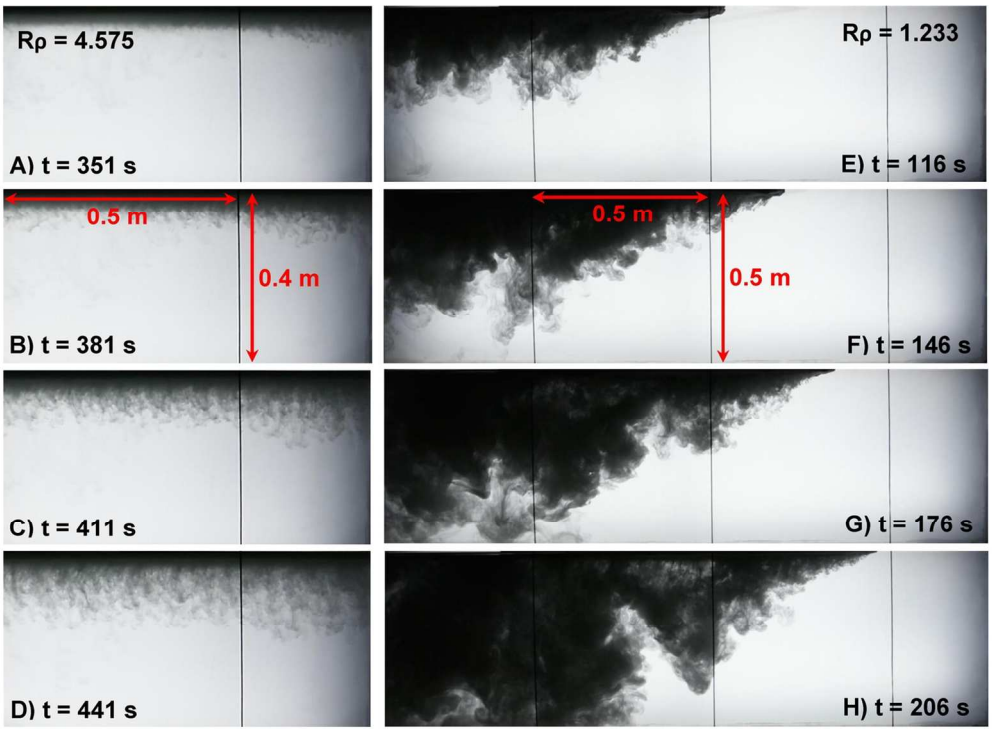

Fig. 5: Close up photos of experimental observations of (A) to (D) slow sinking sediment plumes due to weaker settling-driven convection in an experiment with high R_ρ = 4.575 and (E) to (H) faster sinking sediment fingers due to vigorous settling-driven convection in an experiment with low R_ρ = 1.229.

128x92mm (300 x 300 DPI)

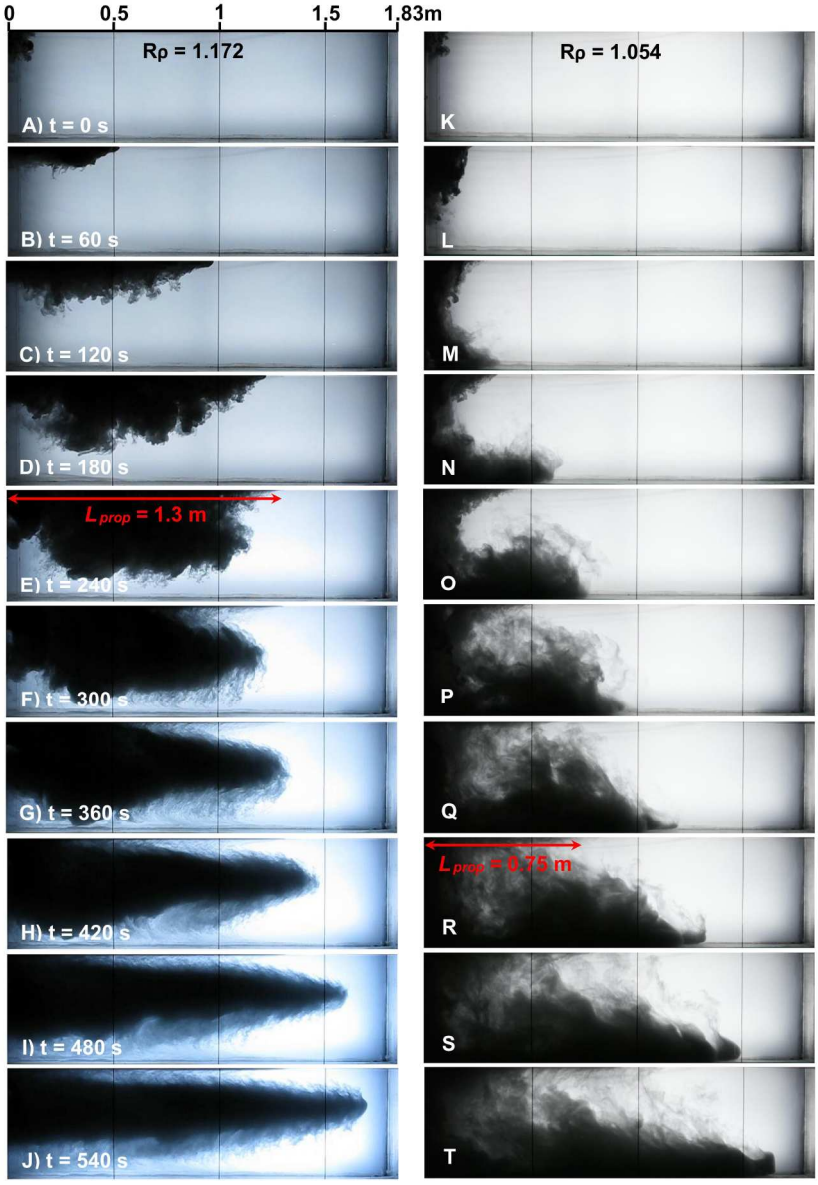

Fig. 6: Photos of experiments showing formation of (A) to (J) an interflow (R_ρ = 1.172) and (K) to (T) an underflow (R_ρ = 1.054) from the descending mixture of sediment and freshwater into saline body.

245x343mm (300 x 300 DPI)

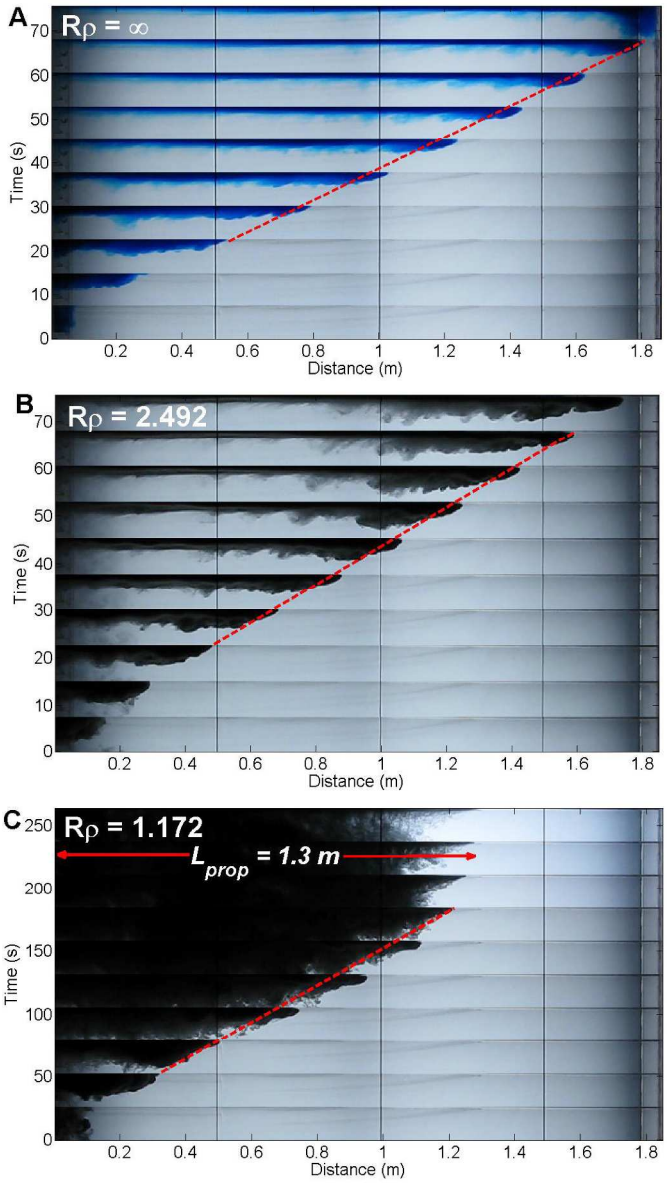

Fig. 7: Comparing the propagation speed of the gravity current for (A) $R_\rho = \infty$ (speed = 0.0279 m/s), (B) $R_\rho = 2.492$ (speed = 0.0246 m/s) and (C) $R_\rho = 1.172$ (speed = 0.0068 m/s).

629x1102mm (300 x 300 DPI)

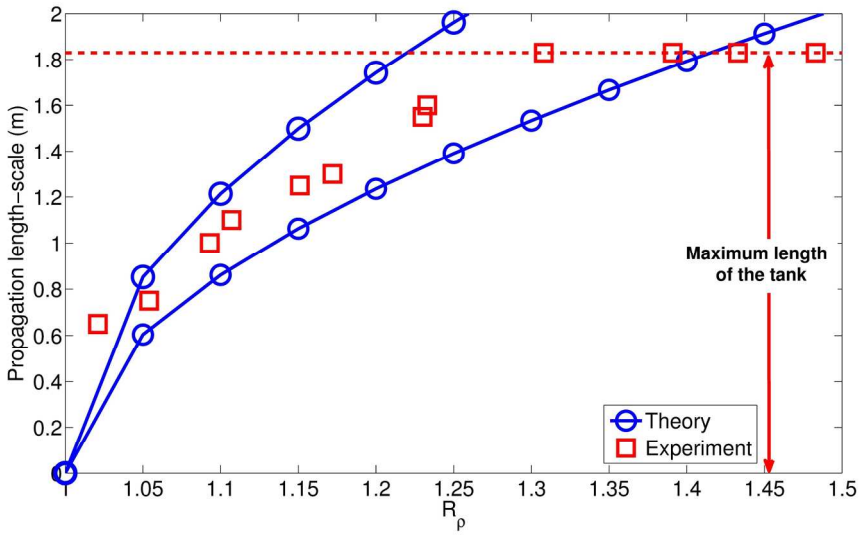

Fig. 8: Comparing theoretical predictions and experimental observations of the propagation length-scale (L_{prop}) of the gravity current as a function of various R_ρ. The two curves for the theory represent a realistic range of values between C_{1avg} = 0.0462 m s^{-1}, C_{2avg} = 0.1489 s, and C_T = 390 and 550 for the coefficient in equation (8). The length of the tank is 1.83 m, limiting the maximum propagation length of the experiments.

188x106mm (300 x 300 DPI)

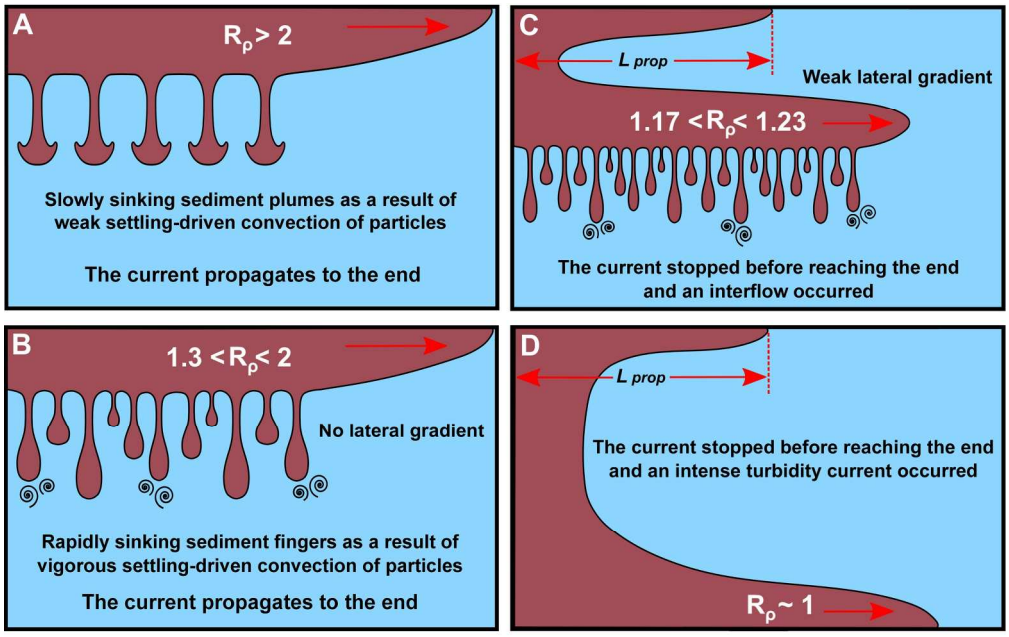

Fig. 9: Schematic figure of the 4 different situations arising in our experiments. (A) Slowly sinking sediment plumes for $R_\rho > 2$, (B) rapidly sinking sediment fingers for $1.3 < R_\rho < 2$, (C) occurrence of an interflow for $1.17 < R_\rho < 1.23$ and (D) occurrence of an intense turbidity current for $R_\rho \sim 1$.

202x127mm (300 x 300 DPI)

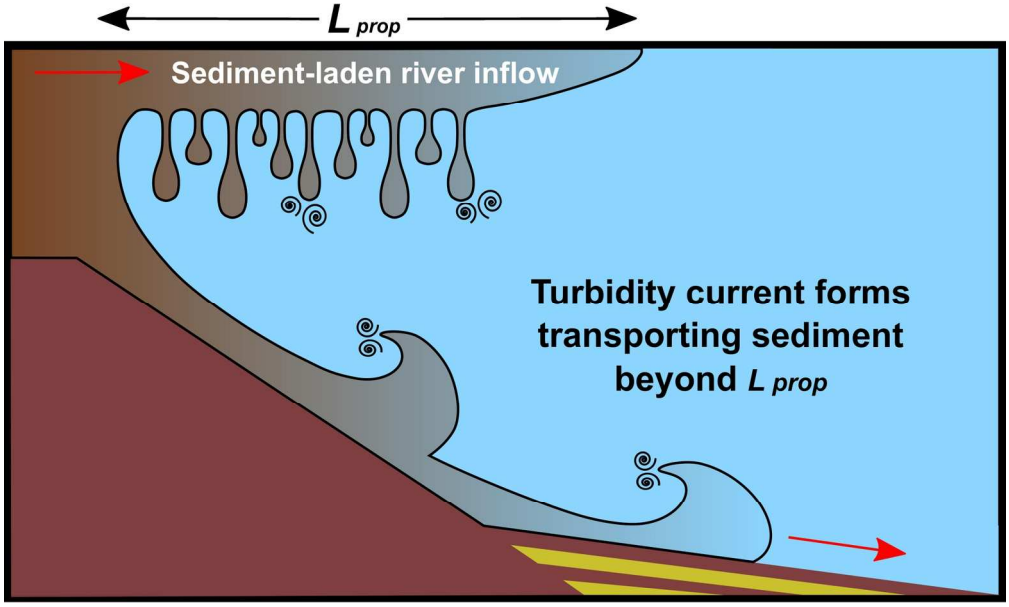

Fig. 10: The rapid loss of sediment from the surface gravity current can potentially form a turbidity current that can propagate distances much greater than L_{prop}. This is the more likely behavior when R_ρ is close to 1, whereas our experiments suggest that Fig. 1 is more relevant for very large R_ρ.

170x102mm (300 x 300 DPI)